IEEE Access
Multidisciplinary | Rapid Review | Open Access Journal

Received January 21, 2020, accepted March 23, 2020, date of publication March 30, 2020, date of current version April 22, 2020.

Digital Object Identifier 10.1109/ACCESS.2020.2984361

Development of a Cross-Type Magnetic Coupler for Unmanned Aerial Vehicle IPT Charging Systems

CHUNWEI CAI[1,2], (Member, IEEE), JINQUAN LIU[1], SHUAI WU[1], YANYU ZHANG[1], LONGYUN JIANG[1], ZHIPENG ZHANG[1], AND JINPENG YU[3], (Member, IEEE)

[1]School of New Energy, Harbin Institute of Technology, Weihai 264209, China
[2]Shandong Institute of Shipbuilding Technology, Weihai 264209, China
[3]School of Automation, Qingdao University, Qingdao 266071, China

Corresponding author: Chunwei Cai (caichunwei@hit.edu.cn)

This work was supported in part by the Natural Science Foundation of Shandong Province of China under Grant ZR2019MEE052, and in part by the Major Scientific and Technological Innovation Project of Shandong Province of China under Grant 2017CXGC0921.

ABSTRACT Inductive power transfer (IPT) is an optimal way for the unmanned aerial vehicle (UAV) wireless charging. The magnetic coupler is the key component in the IPT system, which determines the power transmission capacity and efficiency in IPT system. Due to the particularity of UAV application, the magnetic field height should be strictly limited to avoid the damage caused by high frequency magnetic field heat the UAV's metal equipment. A cross-type magnetic coupler with receiving coil placed on UAV's one landing gear was proposed to solve this problem, but it has the possibility of making UAV fuselage imbalance. Therefore, a novel cross-type magnetic coupler is proposed to overcome its difficulties in this paper, and most of magnetic fields are restrained to be lower than UAV's landing gear height $h_1 = 145$mm, which will not cause damage to the UAV's equipment. And a simple and practical iterative method for designing the magnetic coupler geometry parameters is proposed, with simplification of the complex design process for the finite element analysis, improves the design efficiency. The experimental results show that the system can charge the 260W UAV normally with the system efficiency of 91.577% within the misalignment range of X-axis direction 25mm, Y-axis direction 40mm and rotation 25°.

INDEX TERMS Unmanned aerial vehicle (UAV), inductive power transfer (IPT), cross-type magnetic resonant coupling, magnetic circuit model, coupler geometry parameter design.

I. INTRODUCTION

Unmanned aerial vehicle (UAV) is an aircraft that is controlled by a radio real-time remote control or stored program in advance by itself, capable of carrying multiple functional devices to perform various tasks. It exhibits the advantages such as simple structure, small size, low cost, strong adaptability, flexible to use, etc. It has been applied in scientific research, civils [1] and military fields [2]. However, due to the limitation of volume and bearing capacity, the UAV's battery capacity is limited, and the problem of charging has become a bottleneck in the UAV further development. At present, the manual plug is mainly used to charge the UAV. Obviously, this way has some shortcomings in flexibility, convenience, etc, which reduces the UAV's operation scope, consumes manpower and reduces UAV automation. Therefore, it is important to incorporate the wireless power transfer (WPT) technology to UAV charging technology. WPT technology avoids the direct contact among wires, removes the step of manually plugging and unplugging, improves its operation range and implements the goal of UAV unattended.

Inductive power transfer (IPT) is one of the most widely used methods in the WPT technology. At present, IPT system has been widely used in electric vehicles [3], underwater autonomous vehicles [4], electronic equipment [5], medical devices [6], etc. IPT system consists of two parts, the transmitter and the receiver, which are completely isolated from each other by means of transmitting the electric energy from the transmitter to the receiver wirelessly through a magnetic coupler. The transmitter converts AC voltage with power frequency or DC voltage to high frequency AC voltage through power converter. The high frequency AC current generates

The associate editor coordinating the review of this manuscript and approving it for publication was Ton Do.

a high frequency alternating magnetic field surrounding the transmitting coil through resonant compensation network. The receiving coil picks up most of the alternating magnetic flux and generates the high frequency voltage. The high frequency AC voltage can be converted and adjusted by the power converter so that it can meet the requirements of various loads. By adjusting the circuit parameters and improving the coupling capability, the IPT system can obtain higher transmission power and transmission efficiency.

At present, some scholars have tried to wirelessly charge UAV to improve the UAV's operations scope and achieve the functionality of unattended guard. The method of making air-cored coils around the UAV frame is proposed to implement an IPT system with 35W power and 71% efficiency [7]. As the air gap between the transmitting coil and the receiving coil is large, resulting in the weak coupling capability. But the strong coupling capability is the basis to ensure the efficient wireless power transmission. In order to improve the coupling capability, the receiving coil can be wound around the bottom of the UAV landing gear [8], the receiving coil can be wound around the bottom end of the UAV landing gear. But it causes electromagnetic interference to the battery tank, pan-tilt-zoom camera or other operating equipment installed in the abdomen of the UAV, which will affect performance of the equipment. The high frequency magnetic field heats up the UAV's metal equipment, causing damage to the equipment. Therefore, a scheme with small plane coil installed at the bottom of the landing gear is proposed [9]. Although this scheme solves the electromagnetic interference problem with high coupling capability, the tolerance to misalignment of this scheme is not sufficient. A method is proposed to extend the UAV charging area by using two receiving coils to solve the misalignment tolerance problem [10]. However, the system transmission efficiency is low, only 50%. Due to the limited UAV's space and bearing capacity, it is necessary to reduce the UAV's space occupied by receiver pad and its weight. In [11], the planar air-cored coil is used to reduce magnetic coupler weight, but receiving coil installed on the side of the frame can cause UAV to be unbalanced in operation. Due to limitation of UAV's capacity and landing accuracy, it is important to design a magnetic coupler with strong coupling capability, strong misalignment tolerance and also ensure its receiver pad is of small size and light weight. More importantly, the magnetic field height of magnetic coupler should be strictly limited to avoid the damage caused by the high frequency magnetic field heat the UAV's metal equipment. Therefore, in [12], a cross-type magnetic coupler is proposed, in which the transmitter pad adopts the DD-type structure, and the receiving coil is installed on UAV's one landing gear. The transmitter pad and the receiving coil are perpendicular to each other, and the charging power is 624W, with 90% maximum efficiency. It is suitable for wireless charging for medium power UAV. However, the receiving coil is only wound on UAV's one landing gear, when the turns of receiving coil are more, the coil becomes heavier, which will lead to UAV fuselage imbalance.

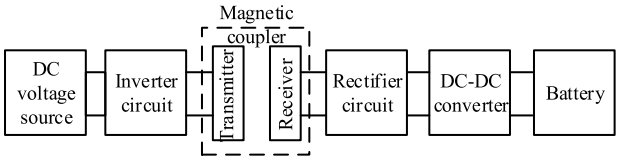

FIGURE 1. A typical IPT system block diagram.

The above researches are focused on magnetic coupler type, and there are only few researches on the design for magnetic coupler geometry parameter at present. In [13], the finite element method is used to carry out repeating simulations and experiments to design the magnetic coupler geometry parameters. Although this method can achieve desired results, it is not universal, and only the coupling coefficient is considered, which can not achieve the balance on multiple design parameters. Therefore, a simple and practical method is needed to design magnetic coupler dimensions.

In contrast to current achievements, a novel cross-type magnetic coupler is proposed in this paper, the main merits of the developed scheme can be summed up as follows:

1) A cross-type magnetic coupler proposed in this paper is proposed, which avoid the influence of high frequency magnetic field on UAV's internal equipment;

2) The magnetic circuit and electric circuit model are established, and a simple and practical iterative method for designing the magnetic coupler geometry parameters is proposed, with simplification of the complex design process, improves the design efficiency.

II. IPT SYSTEM OVERVIEW

A. SYSTEM OVERALL STRUCTURE

A typical IPT system block diagram is shown in Fig. 1. The high frequency sinusoidal current is first generated by DC power supply through the inverter, and the high frequency alternating magnetic field is excited by the transmitter pad. Then the receiver pad receives the electric energy from the primary side by magnetic field coupling to implement the wireless power transmission. The pick-up circuit first converts the high frequency AC voltage into DC voltage through a rectifier circuit, then the voltage and current are adjusted by DC-DC converter to charge the battery.

B. COMPENSATION CIRCUIT SELECTED

In an IPT system, compensation circuit is usually added to compensate for leakage inductance and improve the system transmission efficiency. When voltage source inverter is adopted, the basic compensation structure (primary series and secondary series (SS) [14], [15] or primary series and secondary parallel (SP) [14]–[16] compensation), or the hybrid compensation structure (inductance-capacitance-inductance (LCL) [17] compensation) can be used. Considering that the IPT system in this paper is a low voltage and high current system, if the Boost converter is selected as DC-DC converter, the current fed to the rectifier will be very large resulting in

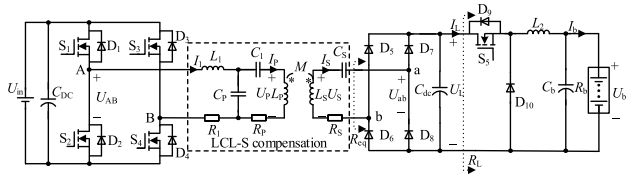

FIGURE 2. Overall circuit diagram of the IPT system for UAV.

considerable loss and low efficiency. The Buck converter can effectively reduce the current level and improve the working efficiency, which is a better scheme of the system in this paper. The Buck converter demand a voltage sourceexcitation, so the SP or the LCL-S compensation can be selected. The reflection impedance of SP compensation is related to the load resistance, by contrast, the reflection impedance of LCL-S compensation is pure resistance, so LCL-S compensation has better stability. Therefore, the LCL-S compensation is selected in this paper. As shown in the dotted line section of Fig. 2.

In Fig. 2, U_{in} is the system input DC voltage, C_{DC}, C_{dc} and C_{b} are filter capacitors, $S_1 \sim S_4$ are inverter switches. L_1 is compensation inductance, C_{P} and C_{S} are the compensation capacitances of the primary and secondary sides, respectively. L_{P} and L_{S} are the inductances of the magnetic coupler primary and secondary sides, respectively. R_1, R_{P} and R_{S} are equivalent internal resistance of coils, $D_5 \sim D_8$ are rectifier diodes. S_5, D_{10} and L_2 constitute Buck converter, and lithium battery is connected finally. In order to improve the secondary induced voltage, a part of L_{P} can be compensated first by adding the compensation capacitance C_1, and then the rest of L_{P} resonates with C_{P}, where $L_1 = L_{\text{P}} - 1/\omega^2 C_1$. It can be obtained that the system output power is as follows [18]:

$$P_{\text{out}} = U_{\text{oc}} I_{\text{sc}} Q_2 = \frac{\omega M^2 I_{\text{P}}^2 Q_2}{L_{\text{S}}} = \frac{k^2 U_{\text{P}}^2 Q_2}{\omega L_{\text{P}}} \tag{1}$$

where, U_{oc} and I_{sc} are the secondary open-circuit voltage and short-circuit current, respectively. $Q_2 = \omega L_{\text{S}}/R_{\text{eq}}$ is the secondary quality factor, U_{P} and I_{P} are the primary excitation voltage and current, respectively. ω is the system resonance angular frequency, M and k are the mutual inductance and the coupling coefficient between the coils, and there is $k = M/\sqrt{L_{\text{P}} L_{\text{S}}}$. The Q_2 is less than 10 generally to improve the system voltage transmission ratio and maintain the system stability [19], so it is constrained to 2-5 in this paper.

C. MAGNETIC COUPLER LIMITATION

From (1), increasing k or decreasing L_{P} will increase the system output power. Therefore, the parameters k and L_{P} of the magnetic coupler are important factors that affect the system output power. k is a key parameter to reflect the magnetic coupler coupling capability, and the magnetic coupler geometry parameter will affect L_{P}. How to ensure higher power transmission capability of magnetic coupler at lower cost is a problem that should be considered. Moreover, the application environment should also be considered in

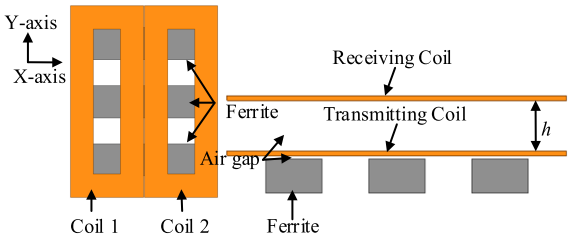

FIGURE 3. The simulation model of DD-type magnetic.

the design of magnetic coupler. Due to limitation of UAV's bearing capacity and landing accuracy, a magnetic coupler should be designed with strong coupling capability, strong misalignment tolerance and its receiver pad takes up less UAV's space and behaves light weight. Therefore, the planar hollow receiving coil is used to reduce receiver pad weight. And the distance between the transmitter pad and the receiver pad is reduced to increase the coupling capability. More importantly, the high frequency alternating magnetic field heats up the UAV's internal metal equipment, resulting in a damage to them. The reference [20] shows that the minimum flux density which causes injury to the human body is 2.7×10^{-5}T, when the system working frequency variation range from 3kHz to 10MH. Human safety standards are often stricter than those for equipment. And the magnetic field height of the magnetic coupler should be strictly limited in this paper. Therefore, the design goal in this paper is that magnetic flux density should be less than 1×10^{-5}T when the height is greater than that of UAV's landing gear height $h_1 = 145$mm, which is smaller than 2.7×10^{-5}T to further ensure the safety of the UAV equipment.

III. NOVEL MAGNETIC COUPLER

A. MAGNETIC COUPLER PROPOSED

As a key part of the IPT system, magnetic coupler's geometry determines the magnetic field pattern and s the system electromagnetic interference level. Enhancing the coupling capability of the magnetic coupler can improve the system power transfer capability. And the system adaptive capability can be improved by reducing the sensitivity of the magnetic coupler to misalignment. At present, the circular pad is one of the most common structure in the literature [18], but the circular pad has the disadvantages of strict air gap requirements and high misalignment sensitivity. Therefore, a DD-type magnetic coupler is proposed [21], which provides a charge zone approximately five times larger than that of the circular pad for a similar material cost, improves the misalignment range and overcomes the difficulty of circular pad. The receiver pad adopts DD-type hollow structure which is installed on the UAV's landing gear to reduce its weight, and the simulation model of DD-type magnetic coupler used in UAV is shown in Fig. 3.

The peak magnetic flux density refers to the magnetic flux density corresponding to the maximum current in the

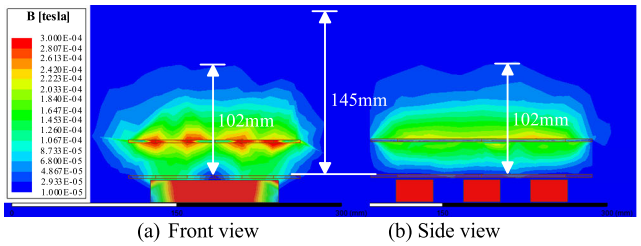

FIGURE 4. Peak magnetic field distribution of DD-type magnetic.

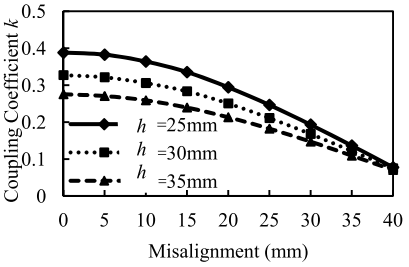

FIGURE 5. Coupling coefficient variation curve with X-axis misalignment.

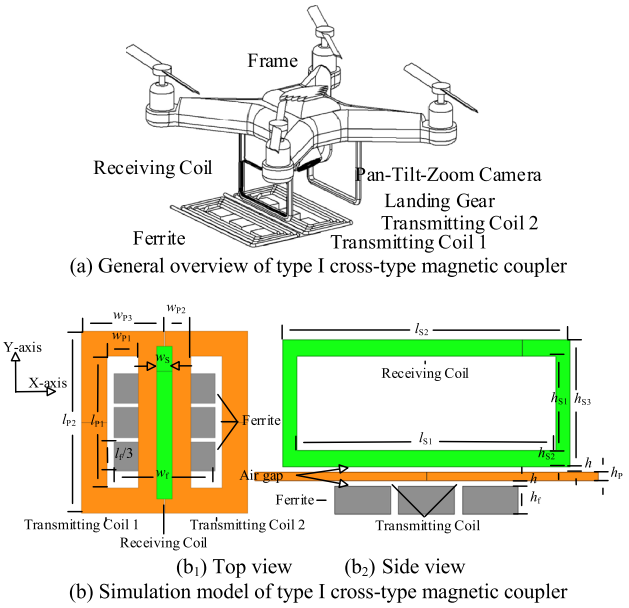

FIGURE 6. Type I cross-type magnetic coupler.

coupling coils, which corresponds to the moment when the high frequency magnetic field has the greatest influence on the UAV internal equipment, and determines the magnetic field safety level of the magnetic coupler. The ampere turns of per transmitting coil is set to 180A·N, and the peak magnetic field distribution of DD-type magnetic coupler is obtained by ANSYS Maxwell software for 3D simulation as shown in Fig. 4. From Fig. 4, the primary excitation current I_P and secondary induced current I_S should be considered in Maxwell simulation. Since both the I_P and the I_S are sine waves, and $I_S = j\omega M I_P/R_{eq}$, the I_P and the I_S phase differ by 90°. The moment of $I_P = I_{Pmax}$ and $I_S = 0$, and the moment of $I_S = I_{Smax}$ and $I_P = 0$ both correspond to the peak magnetic field. the magnetic field distributions in the direction of the receiver pad height are more concerned, and the magnetic field height of the case where $I_S = I_{Smax}$ and $I_P = 0$ is higher than that of the case where $I_P = I_{Pmax}$ and $I_S = 0$. Therefore, the case where $I_S = I_{Smax}$ and $I_P = 0$ is only considered in this paper. The influence of X-axis direction misalignment on the system coupling coefficient when the distance h between the transmitter pad and the receiver pad varies is obtained as shown in Fig. 5.

From Fig. 4, when the height is greater than 88mm, the flux density of the DD-type magnetic coupler is less than 1×10^{-5}T, which meet the requirement for magnetic field height. But the maximum flux density is mainly concentrated on the underside of the receiver pad and the system coupling capability is weak. In order to enhance the coupling capability, the distance h between the transmitter pad and the receiver pad can be reduced. In Fig. 5, reducing h will increase the sensitivity of X-axis misalignment. The magnetic field height can also be increased by increasing the magnetic coupler dimensions to improve the system coupling capability, which will not only increase the cost, but also increase the influence of high frequency magnetic field on the UAV internal equipment. Most UAVs put their landing gears away during flight to allow the camera to rotate the shooting by 360°, which will not block the lens and facilitate aerial photography. Obviously, this DD-type structure is only suitable for fixed landing gear UAVs but not universal. Therefore, in [12], a cross-type magnetic coupler is proposed, as shown in Fig. 6. The transmitter pad adopts the DD-type structure, which is used to expand the UAV wireless charging zone and improve the misalignment range of magnetic coupler, thus reducing the landing accuracy of UAV. A few rectangular ferrite magnetic cores are placed under the transmitting coils, which can not only reduce the leakage of the magnetic coupler, restrain the flux lines better, improve the coupling capability of the magnetic coupler, but also distribute the magnetic field in single-sided direction and eliminate the magnetic shielding device. Due to the particularity of wireless charging for UAV, the receiver pad is required to be light weight and occupy small volume of UAV, which will not affect the UAV's working range. Therefore, the receiving air-core coil is used as the receiver pad to reduce the weight of the receiver pad. The receiving coil is installed on UAV's one landing gear which is perpendicular to the transmitter pad each other and does not occupy the UAV internal space. It not only reduces the distance between the transmitter pad and the receiver pad, improves the coupling capability of the magnetic coupler, but also avoids the high frequency magnetic field heating up the UAV internal metal equipment. However, the receiving coil is only wound on UAV's one landing gear, which will lead to the imbalance of UAV fuselage when the receiving coil gets heavier. Therefore, a novel cross-type magnetic coupler is proposed in this paper, as shown in Fig. 7. The receiving coil is divided into two parts on average which are installed on UAV's two landing gears. These two receiving coils are

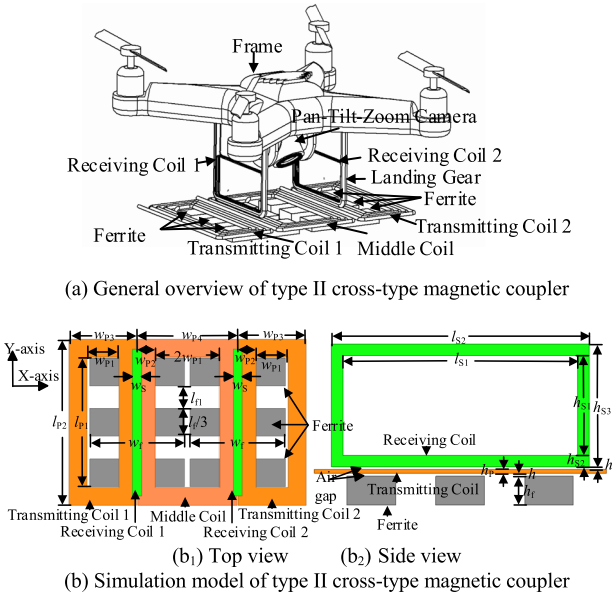

FIGURE 7. Type II cross-type magnetic coupler.

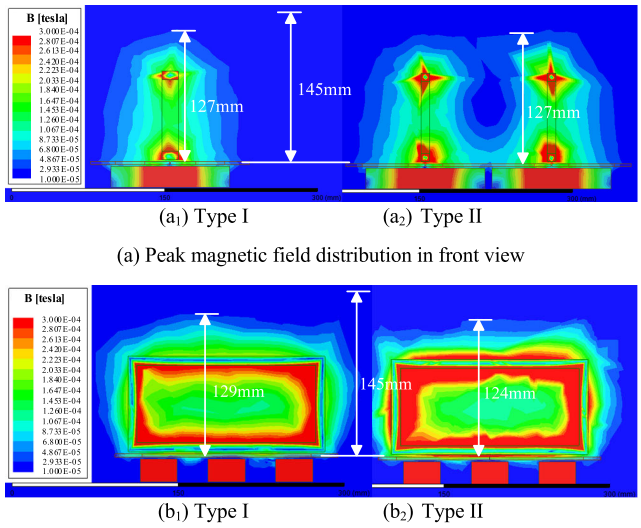

FIGURE 8. Peak magnetic field distribution of two cross-types magnetic coupler.

in series and the coils are wound in the opposite direction. Thus, the problem with imbalance of UAV fuselage caused by overweight of receiving coil is solved. A middle coil is added between the transmitting coil 1 and the transmitting coil 2, and the three transmitting coils are in series which are wound in the same direction. If the current direction flowing through the transmitting coil 1 and the transmitting coil 2 are counterclockwise, the current flowing through the middle coil is clockwise, which not only restrains the direction of flux lines better, but also maintains good characteristics of DD-type magnetic coupler.

High frequency alternating magnetic fields are generated in the process of UAV wireless charging. If the UAV's internal equipment is exposed to such a magnetic field, it will cause electromagnetic interference to these equipment, affect their performance, and even damage the metal equipment. Therefore, the magnetic field height of the magnetic coupler is strictly limited. The ampere turns of the per transmitting coil is set to 180A·N. And the transmitting and receiving coils of the two cross-type magnetic couplers have the same number of turns. The UAV's landing gear height h_l is 145 mm. The peak magnetic field distribution of two cross-types magnetic coupler is obtained by ANSYS Maxwell software for 3D simulation as shown in Fig. 8.

From Fig. 8, when the flux density is less than 1×10^{-5}T, the height of type I is higher 129mm, and the height of type II is higher 127mm, they are all below 145mm. So they are not cause the electromagnetic interference to the UAV's internal equipment. It can be seen that two cross-types magnetic couplers have the almost same level of electromagnetic interference, but compared with type I, type II does not cause UAV fuselage imbalance due to excessive coils.

Due to the limitation that UAV has a low landing accuracy, it is impossible to guarantee that UAV can land on

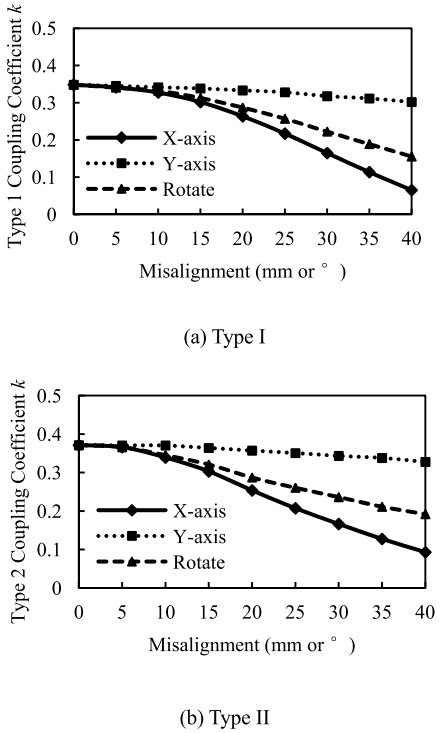

FIGURE 9. The curve of coupling coefficient with misalignment.

the charging platform accurately every time. Therefore, the designed magnetic coupler should have strong misalignment tolerance. When the geometry parameters of the two cross-type magnetic couplers are the same, which include the type and turns of Litz wire used in coupling coils, each ferrite geometry parameters and the frame sizes of each transmitter coil and each receiver coil, the curve of coupling coefficient with misalignment is obtained, as shown in Fig. 9.

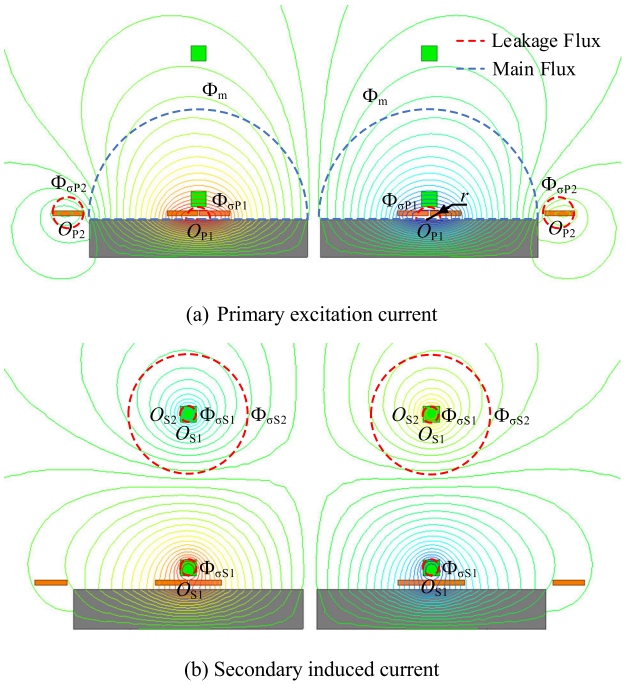

(a) Primary excitation current

(b) Secondary induced current

FIGURE 10. **Magnetic field distribution of the cross-type magnetic coupler.**

In Fig. 9(a) and Fig. 9(b), with the increase of misalignment distance, the coupling coefficient of type I and type II decrease gradually, but the decrease of coupling coefficient of type I is faster than that of type II, indicating that the misalignment sensitivity of type I is higher than that of type II. The coupling coefficient of type I is slightly smaller than that of type II, which indicates that the coupling capability of type I is weaker than that of type II. Therefore, type II cross-type magnetic coupler is selected in this paper.

B. MAGNETIC CIRCUIT MODELING

The magnetic circuit model of the type II cross-type magnetic coupler is established, in order to better study the magnetic field distribution of the magnetic coupler, analyze the influence of the flux lines distribution on the power transmission for wireless charging system, and fundamentally explore the relationship between the system magnetic circuit and the electric circuit. The magnetic field distribution caused by the primary excitation current and the secondary induced current of the cross-type magnetic coupler is shown in Fig. 10.

From Fig. 7(b), l_{P1} and l_{P2} are the inner length and outer length of the transmitting coil, respectively. w_{P1} and w_{P3} are the inner width and outer width of two side transmitting coils, respectively. w_{P2} is the transmitting coil width. w_{P4} is the outer width of the middle coil, and the inner width of the middle coil is twice as wide as that of the two side coils to maintain the symmetry of the magnetic coupler. h_P is the transmitting coil thickness. l_{S1} and l_{S2} are the inner length and outer length of the receiving coil, respectively. w_S is the receiving coil width. h_{S1} and h_{S3} are the inner and outer heights of the receiving coil. h_{S2} is the receiving coil thickness. l_f, w_f and h_f are the length, width and thickness of the rectangular ferrite core, respectively. l_{f1} is the gap between the ferrite cores. h is the air gap between the transmitter pad and receiver pad. The relationship of the magnetic coupler geometry parameters is as follows: $l_{P2} - l_{P1} = 2w_{P2}$, $w_{P3} - w_{P1} = 2w_{P2}$, $w_{P4} - 2w_{P1} = 2w_{P2}$, $l_{S2} - l_{S1} = 2h_{S2}$ and $h_{S3} - h_{S1} = 2h_{S2}$.

In Fig. 10(a), the main flux Φ_m is divided into three parts, one part of flux links partially with the transmitting coil and partially with the receiving coil. Another part of flux links partially with the transmitting coil and fully with the receiving coil. The last part of flux links with all the transmitting coil and all the receiving coil. The flux partially linking with the transmitting coil links with a large part of the transmitting coil, which can be equivalent to the flux linking with all the transmitting coil to simplify the calculation. Therefore, the main flux Φ_m can be equivalent to a concentric semicircle closed along the ferrite core with O_{P1} as the circle center. As shown in the solid line section of Fig. 10(a), the main flux Φ_m equivalent reluctance is R_m. The leakage flux Φ_σ is shown in the dotted line section of Fig. 10(b). The primary leakage flux $\Phi_{\sigma P}$ is divided into three parts. One part of flux can be equivalent to a concentric semicircle closed along the ferrite core with O_{P1} as the circle center, and its equivalent reluctance is $R_{\sigma P1}$. Another part of flux can be equivalent to a concentric circle with O_{P2} as the circle center, and its equivalent reluctance is $R_{\sigma P2}$. These two parts of flux link with the transmitting coil partially but no receiving coil. The last part of flux links with all the transmitting coil but no receiving coil, which is relatively small and can be ignored. The equivalent resistance $R_{\sigma P}$ of primary leakage flux $\Phi_{\sigma P}$ can be regarded as $R_{\sigma P1}$ is connected in parallel with $R_{\sigma P2}$. The secondary leakage flux $\Phi_{\sigma S}$ is divided into two parts. One part of flux links with the receiving coil partially but no transmitting coil, which can be equivalent to a concentric circle with O_{S1} as the circle center, and its equivalent reluctance is $R_{\sigma S1}$. The other part of flux links with all the receiving coil but no transmitting coil, which can be equivalent to a concentric circle with O_{S2} as the circle center, and its equivalent reluctance is $R_{\sigma S2}$. The equivalent resistance $R_{\sigma S}$ of secondary leakage flux $\Phi_{\sigma S}$ which can be regarded as $R_{\sigma S1}$ is connected in parallel with $R_{\sigma S2}$.

Reluctance is a parameter describing the flux conduction capability of the magnetic circuit, and its effect is similar to that of the resistance in the circuit model. The reluctance magnitude is subject to the structure and size of magnetic coupler and the material permeability [22]. The reluctance with magnetic circuit equivalent length l can be expressed as follows:

$$R_i = \frac{l}{\mu_a S} \tag{2}$$

where S is the flux equivalent cross-sectional area, μ_a is the permeability of material a. The permeability of ferrite material is much larger than that of air, so the reluctance of ferrite core is much smaller than that of air and can be ignored.

Taking the calculation of reluctance $R_{\sigma P1}$ as an example, the magnetic circuit modeling method is introduced.

In Fig. 10, according to the formula (2), the differential reluctance $dR_{\sigma P1}$ along the radius r direction can be obtained as follows:

$$dR_{\sigma P1} = \frac{\pi r}{\mu_0 \cdot 2l_f dr} = \frac{\pi r}{2\mu_0 l_f dr} \tag{3}$$

where μ_0 is the permeability of air, and the value is $\mu_0 = 4\pi \times 10^{-7}$H/m. The transmitting coil turns $N_{\sigma P1}$ surrounded by the differential element can be approximately expressed as:

$$N_{\sigma P1} = \frac{2r}{2w_{P2}} \cdot N_P = \frac{r}{w_{P2}} \cdot N_P \tag{4}$$

where N_P is the transmitting coil turns. According to the Ohm's law of magnetic circuit, the following can be obtained:

$$N_{\sigma P1} I_P = d\Phi_{\sigma P1} dR_{\sigma P1} \tag{5}$$

Substituting (3), (4) into (5), the differential magnetic flux $d\Phi_{\sigma P}$ is obtained as:

$$d\Phi_{\sigma P1} = \frac{N_{\sigma P1} I_p}{dR_{\sigma P1}} = \frac{2\mu_0 l_f N_P I_P dr}{\pi w_{P2}} \tag{6}$$

According to the principle of flux linkage equality, the primary equivalent leakage flux linkage which can be equivalent to a concentric semicircle closed along the ferrite core with O_{P1} as the circle center can be obtained as follows:

$$\Psi_{\sigma P1} = N_P \Phi_{\sigma P1} = \int N_{\sigma P1} d\Phi_{\sigma P1} \tag{7}$$

Formula (4), (6) and (7) simultaneous, we can obtain the primary equivalent leakage flux $\Phi_{\sigma P1}$ which can be equivalent to a concentric semicircle closed along the ferrite core with O_{P1} as the circle center:

$$\Phi_{\sigma P1} = \frac{2\mu_0 l_f N_P I_P}{\pi w_{P2}^2} \int_0^{h_P+2h} rdr = \frac{\mu_0 l_f (h_P + 2h)^2 N_P I_P}{\pi w_{P2}^2} \tag{8}$$

At the same time, according to the Ohm's law of magnetic circuit, the magnetomotive force of transmitting coil can be obtained as follows:

$$F = N_P I_P = \Phi_{\sigma P1} R_{\sigma P1} \tag{9}$$

From (8) and (9), the equivalent reluctance $R_{\sigma P1}$ is obtained as:

$$R_{\sigma P1} = \frac{N_P I_P}{\Phi_{\sigma P1}} = \frac{\pi w_{P2}^2}{\mu_0 l_f (h_P + 2h)^2} \tag{10}$$

Similarly, the corresponding reluctance calculation results are shown in Table 1.

The equivalent magnetic circuit of the cross-type magnetic coupler in Fig. 8 can finally be obtained as shown in Fig. 11.

N_S is the receiving coil turns. In Fig. 11, that equivalent magnetic circuit is divided into three sub-loops, which is α, β and γ. The sub-loop α represents the flux only passes through the transmitter pad, so it corresponds to the primary leakage magnetic circuit. The sub-loop β represents the flux passes through both the transmitter pad and the receiver pad, so it corresponds to the magnetizing circuit. Similarly, the sub-loop γ represents the flux only through the receiver pad, so it corresponds to the secondary leakage magnetic circuit.

TABLE 1. Corresponding reluctance calculation results.

Parameters	Expression
Reluctance $R_{\sigma P1}$	$\frac{\pi w_{P2}^2}{\mu_0 l_f (h_P+2h)^2}$
Reluctance $R_{\sigma P2}$	$\frac{2\pi}{\mu_0 (l_{P2}+4w_{P1}+4w_{P2})}$
Primary leakage flux equivalent reluctance $R_{\sigma P}$	$R_{\sigma P1} \parallel R_{\sigma P2}$
Main flux equivalent reluctance R_m	$\frac{2\pi}{\mu_0 l_f \ln\frac{w_f}{2h_P+4h}}$
Reluctance $R_{\sigma S1}$	$\frac{4\pi}{\mu_0 (l_{S2}+h_{S1})}$
Reluctance $R_{\sigma S2}$	$\frac{4\pi}{\mu_0 (l_{S2}+2h_{S1}+h_{S2}) \ln\frac{h_{S3}-h_{S2}}{w_S}}$
Secondary leakage flux equivalent reluctance $R_{\sigma S}$	$R_{\sigma S1} \parallel R_{\sigma S2}$

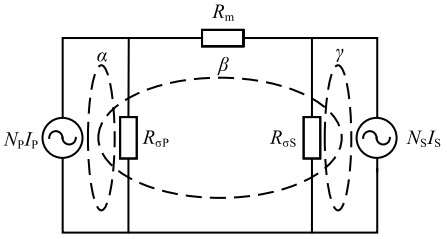

FIGURE 11. Equivalent magnetic circuit of the cross-type magnetic coupler.

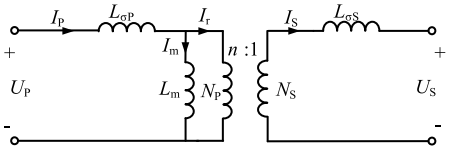

FIGURE 12. Equivalent circuit of the magnetic coupler.

The relationship between the corresponding reluctance and the inductance can be calculated as follows:

$$\begin{cases} L_{\sigma P} = \dfrac{N_P^2}{R_{\sigma P}} \\ L_m = \dfrac{N_P N_S}{R_m} \\ L_{\sigma S} = \dfrac{N_S^2}{R_{\sigma S}} \end{cases} \tag{11}$$

where L_m is the magnetizing inductance, $L_{\sigma P}$ and $L_{\sigma S}$ are the primary leakage inductance and the secondary leakage inductance, respectively. In order to express the circuit relationship of the corresponding inductance more clearly, the equivalent magnetic circuit in Fig. 11 can be converted into the circuit in Fig. 12.

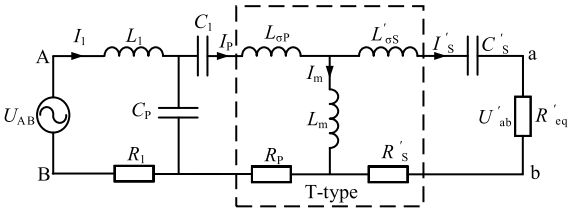

FIGURE 13. T-type equivalent circuit of the magnetic coupler.

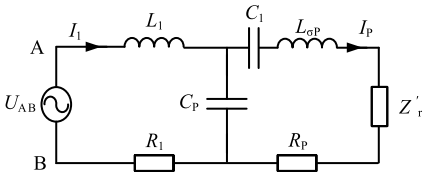

FIGURE 14. LCL-S compensation primary equivalent circuit.

From Fig. 12, the circuit consists of a magnetizing circuit and an ideal transformer with variable ratio n, where $n = N_P/N_S$, and it ignores the internal resistance of the magnetic coupling coils.

C. SYSTEM CIRCUIT MODELING

When the parasitic resistance of the coils should be taken into consideration and the LCL-S compensation described above is added in Fig. 12, the T-type equivalent circuit which is converted to the primary side is obtained, as shown in Fig. 13. The variables relationship between the secondary side and the primary side is as follows:

$$\begin{cases} U_2' = nU_2 \\ I_2' = I_2/n \\ Z_2' = n^2 Z_2 \end{cases} \tag{12}$$

From (12), U_2, I_2 and Z_2 are the voltage, current and impedance of the secondary side, respectively. U_2', I_2' and Z_2' are the voltage, current and impedance converted from the secondary side to the primary side, respectively.

In Fig. 13, the conversion relationship between the primary leakage inductance $L_{\sigma P}$, the secondary leakage inductance $L_{\sigma S}$ and the magnetizing inductance L_m and the primary self-inductance L_P, the secondary self-inductance L_S and mutual inductance M described above are as follows:

$$\begin{cases} L_P = L_{\sigma P} + L_m \\ L_S = L_{\sigma S} + L_m/n^2 \\ M = L_m/n \end{cases} \tag{13}$$

According to formula (13), when the parasitic resistance of the coils and compensation structure are considered, the circuit in Fig. 13 can be equivalent to the mutual coupling circuit shown in Fig. 2, and thus the circuit model is unified with the magnetic circuit model. In this paper, the compensation inductance and magnetic coupler are wound by Litz wires, and its parasitic resistance is very small. Therefore, the parasitic resistance of the compensation inductor and coupling coil can be ignored in the analysis process.

From Fig. 13, the total impedance of the secondary circuit can be expressed as

$$Z_S = j\omega L_{\sigma S} + \frac{1}{j\omega C_S} + R_{eq} \tag{14}$$

In order to achieve maximum output power and transmission efficiency, meanwhile minimizing the VA rating of the power supply, the system should operate at resonant. When the secondary circuit resonates, the L_m is converted to the secondary side. The resonant frequency ω is

$$\omega = \frac{1}{\sqrt{\left(L_{\sigma S} + L_m/n^2\right) C_S}} \tag{15}$$

Now secondary circuit total impedance changes to

$$Z_S = R_{eq} - j\omega L_m \Big/ n^2 \tag{16}$$

Z_S is converted to the primary side to get:

$$Z_S' = n^2 Z_S = R_{eq}' - j\omega L_m \tag{17}$$

The reflect impedance of the secondary circuit equivalent to the primary side is

$$Z_r' = j\omega L_m \parallel Z_S' = \frac{\omega^2 L_m^2 + j\omega L_m R_{eq}'}{R_{eq}'} \tag{18}$$

Therefore, Fig. 13 circuit can be equivalent to primary equivalent circuit as shown in Fig. 14.

From Fig. 14, the total impedance of primary circuit is

$$\begin{aligned} Z_P &= j\omega L_1 + \frac{1}{j\omega C_P} // \left(j\omega L_{\sigma P1} + Z_r'\right) \\ &= \frac{Z_r'\left(1 - \omega^2 C_P L_1\right) + j\omega\left[(L_1 + L_{\sigma P1}) - \omega^2 C_P L_1 L_{\sigma P1}\right]}{\left(1 - \omega^2 C_P L_{\sigma P1}\right) + j\omega C_P Z_r'} \end{aligned} \tag{19}$$

where $L_{\sigma P1} = L_{\sigma P}\text{-}1/\omega^2 C_1$, which is the residual leakage inductance of $L_{\sigma P}$ compensated by C_1.

In Fig. 13, when the primary circuit resonates, the resonance frequency is the same as the secondary circuit, that is

$$\omega = \frac{1}{\sqrt{(L_{\sigma P1} + L_m)\, C_P}} \tag{20}$$

$L_1 = L_{\sigma P1} + L_m$. The primary circuit total impedance is

$$Z_P = \frac{j\omega L_1^2}{L_m + j\omega C_P Z_r' L_1} \tag{21}$$

As can be seen from Fig. 14 and combine with formula (13). The excitation current flowing through the primary circuit is

$$I_P = \frac{U_{AB}}{Z_P} \cdot \frac{\frac{1}{j\omega C_P}}{\frac{1}{j\omega C_P} + \left(j\omega L_{\sigma P1} + Z_r'\right)} = \frac{U_{AB}}{j\omega L_1} \tag{22}$$

From formula (22), the primary compensation inductance does not change during the process of UAV static charging.

As long as the inverter output voltage and the system resonant frequency are constant, the primary excitation current can be kept constant, and thus the energy can be transferred steadily to the secondary side. The voltage of reflect impedance Z_r' is

$$U_r' = I_P Z_r' = \frac{U_{AB}\left(\omega^2 L_m^2 + j\omega L_m R_{eq}'\right)}{j\omega L_1 R_{eq}'} \tag{23}$$

When the secondary side is operated at resonant frequency and combine with formula (13), the rectifier input voltage of the secondary side converted to the primary side is as follows

$$U_{ab}' = U_r' \cdot \frac{R_{eq}'}{Z_S'} = \frac{L_m U_{AB}}{L_1} \tag{24}$$

U_{ab}' is converted to the secondary side to get:

$$U_{ab} = \frac{U_{ab}'}{n} = \frac{L_m U_{AB}}{n L_1} = \frac{M U_{AB}}{L_1} \tag{25}$$

It can be seen from formula (25) that the primary compensation inductance and mutual inductance remain unchanged in the process of static wireless charging. As long as the inverter output voltage is constant, the rectifier input voltage can be guaranteed to be constant and the characteristics of the voltage source can be obtained. The rectifier input voltage can be improved by properly increasing the ratio of mutual inductance to primary compensation inductance.

In order to analyze easily the influence of the primary and the secondary self-inductances on the system output power and efficiency, the proportional coefficient λ of the primary compensation inductance L_1 and the primary self-inductance L_P is defined as follows:

$$\lambda = \frac{L_1}{L_P} \tag{26}$$

When the resistance of the coils is considered and combine with formula (13) and (26), the rectifier output power and efficiency are obtained as shown in formula (27) and (28), respectively.

$$P_{out} = \frac{|U_{ab}|^2}{R_{eq}} = \frac{M^2 U_{AB}^2 R_{eq}}{A^2} \tag{27}$$

$$\begin{aligned}\eta_{out} &= \frac{|I_S|^2 R_{eq}}{|I_S|^2 R_{eq} + |I_S|^2 R_S + |I_P|^2 R_P + |I_1|^2 R_1} \\ &= \frac{\omega^2 M^2 R_{eq}}{\omega^2 M^2 \left(R_{eq} + R_S\right) + R_P \left(R_{eq} + R_S\right)^2 + \omega^2 B^2 R_1}\end{aligned} \tag{28}$$

$$A = (\lambda L_P + C_P R_1 R_P)\left(R_{eq} + R_S\right) + \omega^2 M^2 C_P R_1 \tag{29}$$

$$B = C_P\left[R_P\left(R_{eq} + R_S\right) + \omega^2 M^2\right] \tag{30}$$

In Fig. 2, the system resonant network only allows the fundamental harmonic to pass, which plays the role of band-pass filter, and thus it only needs to consider the fundamental harmonic in the analysis. For static wireless charging, the inverter can adopt complementary control mode with 180°. The fundamental effective value of the inverter output voltage can be obtained by fourier decomposition [23].

$$U_{AB} = \frac{2\sqrt{2}}{\pi} U_{in} \tag{31}$$

In (31), U_{in} is the system input DC voltage. Since the output of LCL-S compensation structure is of a voltage source characteristic and the rectifier requires a large capacitance in parallel to smooth the output voltage, therefore, the relationship between the input and output equivalent load resistance R_{eq} and R_L of the rectifier is as follows [24]:

$$R_{eq} = \frac{8}{\pi^2} R_L \tag{32}$$

In order to better analyze the characteristics of lithium battery, the electrical model of lithium battery is established [25]. However, it is difficult to determine the parameters in the equivalent circuit model of lithium battery. The battery is usually equivalent to a varying resistance. U_b and I_b are charging voltage and current for the battery, respectively. R_b is equivalent resistance of the battery. The rectifier output voltage U_L is approximately constant in the charging process, but the equivalent charging resistance R_b will change. Therefore, the charging voltage U_b and charging current I_b can meet the battery charging requirements by adjusting the duty cycle D of the switch S_5. The output equivalent load resistance R_L of the rectifier is obtained as follows:

$$R_L = \frac{R_b}{D^2} \tag{33}$$

TABLE 2. Specific design requirements of IPT system.

Parameters	*Value*
DC voltage source U_{in}/V	84
Working frequency of the inverter circuit f/kHz	50
DC-DC converter input voltage U_L/V	40-48
Lithium battery capacity C_b/mAh	10000
Nominal voltage for lithium battery U_{bN}/V	22.2
Maximum charging voltage for lithium battery U_{bmax}/V	25.2
Charging current for lithium battery I_b/A	5-10
Charging power for lithium battery P_b/W	126-252

IV. MAGNETIC COUPLER DESIGN

A. DESIGN INDEX PROPOSED

In this paper, 84V DC voltage source is used as the system input voltage. This paper adopts a single phase voltage inverter and a constant frequency control mode to keep the inverter frequency f constant at 50kHz, and the system circuit can always be operated in the resonance state. The single phase uncontrollable rectifier and Buck circuit are selected as the secondary power management circuit. The input voltage range of DC-DC converter is required from 40V to 48V. The battery of UAV adopts lithium battery whose capacity is 10000mAh, nominal voltage is 22.2V, maximum charging voltage is 25.2V, and the required charging rate is from 0.5C to 1C. The specific design requirements are shown in Table 2.

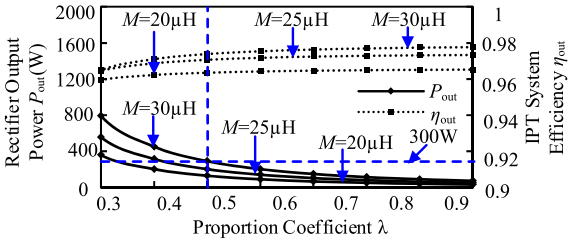

FIGURE 15. Relationship curve between P_{out}, η_{out} and λ with different M.

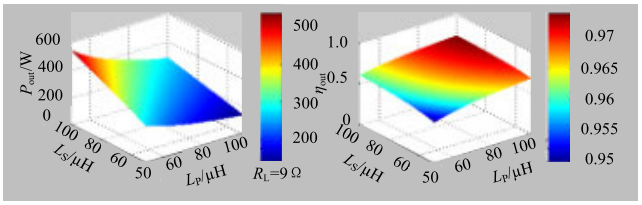

FIGURE 16. Three-dimensional scanning diagram by MATLAB.

The coupling coefficient k of the magnetic coupler designed in this paper should be more than 0.3. Considering that the Buck circuit will produce about 4% loss, the output power range of the rectifier output equivalent load resistance R_L is from 131.25W to 262.5W, and considering the loss of inverter and rectifier, there should be a certain margin for the rectifier output power. Therefore, the rectifier maximum output power is approximately 300W and the output efficiency is more than 90% to meet the battery charging requirements.

From formulas (27) and (28), the proportional coefficient λ will affect the output power and efficiency of the rectifier. Selecting the appropriate proportional coefficient λ can not only improve the secondary induced voltage to improve the system power transmission capability, but also weigh the rectifier output power and efficiency, which can be maintained in a high level. When the different mutual inductances M are selected, the relationship between the rectifier output power P_{out}, efficiency η_{out} and the proportional coefficient λ is shown in Fig. 15.

In Fig. 15, with the increase of the λ, the rectifier output power decreases gradually and approaches to stability, but the IPT system efficiency increases gradually and tends to be stable. The proportional coefficient λ should be chosen where the rectifier output power and efficiency are high and stable. Therefore, in this paper, $\lambda = 0.5$, that is, $L_1 = 0.5L_P$.

From Fig. 2 and formula (27)-(33), assuming that the coupling coefficient k is 0.3, the resistance of the coils and compensation inductance are 0.1Ω. The system input DC voltage U_{in} is 84V, and the proportional coefficient λ is 0.5. When the magnetic coupler is in a well-aligned condition, the DC-DC converter input voltage U_L is 48V. The battery is charged with the maximum charging current I_{bmax} of 10A until the maximum charging voltage U_{bmax} of 25.2V is reached. So the equivalent load resistance of the charged battery $R_b = 25.2V/10A=2.52\Omega$ at the maximum charging power point P_{bmax} of 252W, and the duty cycle of the switch $S_5 D = 25.2V/48V=0.525$. According to formula (33), when the equivalent load resistance of the rectifier R_L is 9Ω ($2.52\Omega/0.525^2 = 9\Omega$), the transferred power to the battery corresponds to the maximum point. Therefore, a load resistance of 9Ω can be used to evaluate the system performance very well. The primary excitation voltage U_P cannot exceed 400V due to the limitation of insulation and safety standards in this paper. And the primary excitation current I_P should be below 12A to limit the I^2R losses. According to the formula (22), (26), (31) and $L_P = U_P/j\omega I_P$, the variation range of the primary self-inductance L_P is calculated to be 40-106μH. Considering a certain safety margin, the variation range of the L_P is 50-100μH. According to formula (32), the input equivalent load resistance R_{eq} at the maximum charging power point is 7.3Ω. In this paper, the secondary quality factor Q_2 is 2-5, and combined with $L_S = Q_2 R_{eq}/\omega$, the variation range of secondary self-inductance L_S is 46-116μH. Considering a certain margin, the variation range of L_S is 50-100μH. According to formula (27)-(30). when the R_L is 9Ω, the three-dimensional scanning diagram of the rectifier output power and efficiency with magnetic coupler self-inductances is obtained by MATLAB as shown in Fig. 16. The rectifier output power and efficiency increase with the decrease of R_L and L_P but the increase of L_S. When the R_L is 9Ω, the L_P changes from 71.7μH to 100μH and the L_S changes from 50μH to 84.2μH, the rectifier output power varies approximately from 138.2W to 318.6W and the output efficiency is more than 90%, which can meet the requirements of the rectifier output power and efficiency.

B. GEOMETRY PARAMETERS DESIGN

As one of the key components of IPT system, the magnetic coupler geometry parameters includes multiple parameters, which is closely related to the system power transfer capability. And the system output power and efficiency are important parameters reflecting the system power transfer capability. The trade-off of the multiple geometry parameters and the system output power and efficiency can save the cost of manufacturing the magnetic coupler, and also ensure the system power transfer capability. In this paper, an iterative method is proposed to optimize the magnetic coupler geometry parameters. Firstly, the variation range of the primary and secondary self-inductances are obtained according to the design index of the system output power and efficiency, and then the relationship of the self-inductance, mutual inductance and the magnetic coupler geometry parameters are obtained according to the magnetic circuit model. Then the geometry parameters satisfying requirements are screened out by the iterative method, and the output power and efficiency corresponding to these geometry parameters are compared one by one to determine the final geometry parameters of the magnetic coupler. And the design considering the magnetic coupler geometry parameters and the system output power and efficiency is completed. The specific method is as follows:

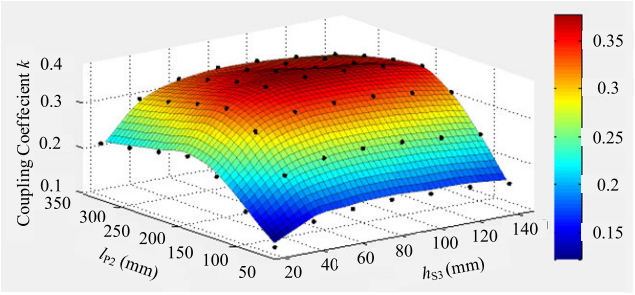

FIGURE 17. Relationship curve between l_{P2}, h_{S3} and k.

From Fig. 7 (b), the Litz wire with size of 0.1mm×400 is adopted and its equivalent diameter d is 2.75mm. The transmitting coil is wound up one layer, and its thickness h_P is 2.75mm. The receiving coil is wound up three layers to reduce the UAV landing gear space occupied by the receiving coil, and its thickness h_{S2} is 8.25mm. The air gap h between the transmitter pad and receiver pad is 2mm. According to the UAV's space limitation, constraints of the magnetic coupler geometry parameters are obtained as follows:

Because the receiving coil is installed on UAV's two landing gears, some geometry parameters of magnetic coupler will be limited. The length of the UAV landing gear is 180mm, so the l_{S2} is set as 180mm accordingly. At this time, the l_{P2} should choose the appropriate range according to l_{S2}. For receiving coil, l_{P2} is too long to fully receive the magnetic field generated by the transmitter pad. And if l_{P2} is too short, the Y-axis direction misalignment tolerance of magnetic coupler will be insufficient. So l_{P2} is required to vary from 50mm to 350mm. Similarly, the distance between the UAV's two landing gears is 124 mm, so the middle coil outer width w_{P4} is 124 mm. The receiving coil outer height h_{S3} should also be reasonably selected according to w_{P4}, which should not exceed the UAV's landing gear height h_l. The coupling capability of the magnetic coupler will be reduced due to the lack of the magnetic field received by the receiving coil, caused by low h_{S3}. If h_{S3} is too high and the secondary leakage flux will cause electromagnetic interference to the UAV. Therefore, the variation range of h_{S3} is from 20mm to 140mm. And the coupling coefficient k is an important parameter to reflect the coupling capability of the magnetic coupler. Therefore, the influence of the l_{P2} and the h_{S3} variation on the k can be studied, respectively, to determine the appropriate values of l_{P2} and h_{S3}, as shown in Fig. 17.

In Fig. 17, with the increase of l_{P2} and h_{S3}, the k increases at first and then decreases gradually. When $l_{P2} = 204$mm and $h_{S3} = 87$mm, the k reaches the maximum value. Therefore, the transmitting coil outer length l_{P2} is 204mm and the receiving coil outer height h_{S3} is 87mm to improve the coupling capability. The ferrite core dimension is also an important aspect to be considered. The rectangular ferrite core dimension is too small to restrain the flux lines, leading to the lack of coupling capability of the magnetic coupler. While the rectangular ferrite core dimension is so large to waste the ferrite core material. Therefore, the rectangular ferrite core length l_f varies from 92mm to l_{P1}, and the rectangular ferrite core width w_f varies from 108mm to $2(w_{P1} + w_{P2})$. According to the magnetic circuit model established above, the self-inductance and mutual inductance of magnetic coupler are independent with the rectangular ferrite core thickness h_f. In order to save the ferrite core material, a thinner core can be chosen as far as possible, so the rectangular ferrite core with the thickness $h_f = 17$mm can be selected.

Assuming N_{P1} is the per transmitting coil turns and N_{S1} is the per layer turns of each receiving coil. $N_P = 3N_{P1}$, $N_S = 6N_{S1}$. The N_{P1} range is 4-10 turns, and the N_{S1} range is 1-7 turns. According to the relationship of the magnetic coupler geometry parameters in Fig. 7(b), we can get $h_{S1} = 70.5$mm and $l_{S1} = 163.5$mm. The following relationship can be obtained:

$$w_{P2} = 2.75 \times 10^{-3} N_{P1} \tag{34}$$
$$w_S = 2.75 \times 10^{-3} N_{S1} \tag{35}$$
$$l_{P1} = 0.204 - 5.5 \times 10^{-3} N_{P1} \tag{36}$$
$$w_{P3} = 2.75 \times 10^{-3} N_{P1} + 0.062 \tag{37}$$
$$w_{P1} = w_{P3} - 5.5 \times 10^{-3} N_{P1} \tag{38}$$

Combined with the expression of the corresponding reluctance in Table 1, as well as formulas (11) and (13), the relationship between self-inductance and mutual inductance of magnetic coupler and various dimensions can be obtained as follows:

$$M = \left[3.6 \times 10^{-6} N_{P1} N_{S1} l_f \ln\left(w_f / 0.0135\right)\right] / n \tag{39}$$
$$L_P = nM + m_1 \tag{40}$$
$$L_S = M/n + m_2 \tag{41}$$

In (40) and (41), respectively, m_1 represents $1.8 \times 10^{-6} N_{P1}^2 (4w_{P1} + 0.011N_{P1} + 0.204) + 2.169 \times 10^{-5} l_f$ and m_2 represents $3.6 \times 10^{-6} N_{S1}^2 [0.329 \ln(28.636/N_{S1}) + 0.251]$. According to the relationship between the electric circuit model and the magnetic circuit model, the appropriate geometry parameters of the magnetic coupler are designed. The flowchart for the geometry parameters design of the magnetic coupler is shown in Fig. 18.

The program in Fig. 18 is written by Visual C++, and the iterative operation is carried out. The geometry parameters of the magnetic coupler that satisfy the requirements can be selected efficiently, and the specific parameters are shown in Table 3.

The relationship between the data of each group in Table 3 and the rectifier output power P_{out} and efficiency η_{out} is obtained by substituting the data of each group in Table 3 into (27) and (28), as shown in Fig. 19.

From Fig. 19, the theoretical value of the IPT system efficiency with each group is more than 96%, because the loss of the inverter and rectifier are ignored. In this paper, the rectifier maximum output power is 262.5W, and considering the loss of inverter and rectifier, there should be

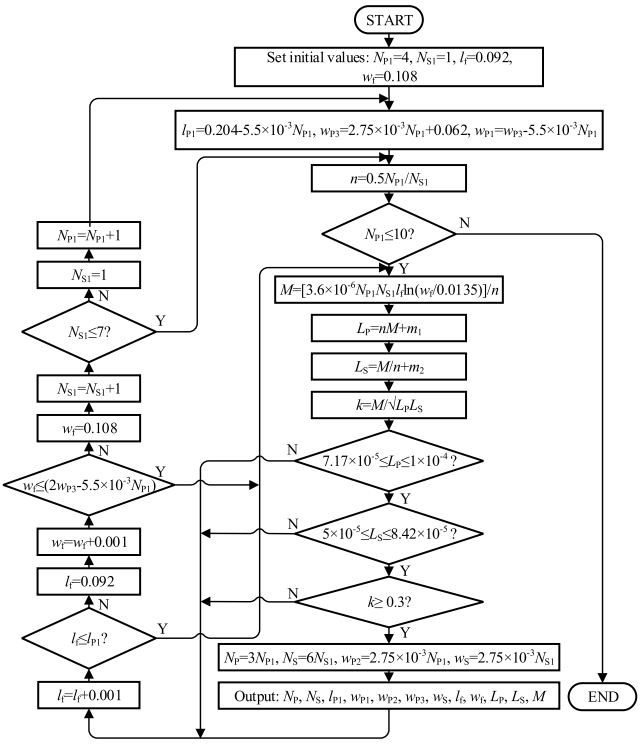

FIGURE 18. Flowchart for magnetic coupler geometry parameters design.

TABLE 3. Output result with iterative method.

Group	N_P	N_S	l_f/mm	w_f/mn	L_P/μH	L_S/μH	M/μH
1	24	24	102	108	78.7	76.2	24.4
2	24	24	112	108	81.3	78.6	26.8
3	24	24	122	108	83.9	81	29.2
4	24	24	132	108	86.6	83.4	31.6
5	24	24	92	118	77	74.7	23
6	24	24	102	118	79.8	77.2	25.5
7	24	24	112	118	82.5	79.7	28
8	24	24	122	118	85.2	82.2	30.5
9	27	24	112	108	98.5	75.6	26.8
10	27	24	102	118	96.8	74.4	25.5
11	27	24	112	118	99.8	76.6	28

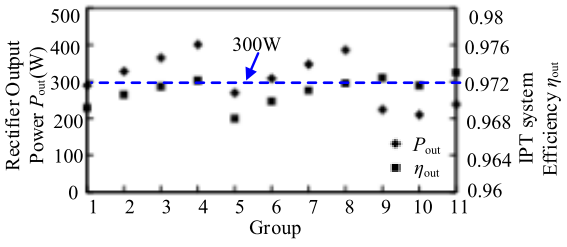

FIGURE 19. Relationship between data of each group and P_{out} and η_{out}.

a certain margin for the rectifier output power. Therefore, it should be selected that group which the rectifier output power is approximately 300W, so the 6th group is selected as the geometry parameters of magnetic coupler, whose rectifier output power is 307.95W and efficiency is 96.98%. Considering synthetically coupling capability, self-inductance value,

TABLE 4. Parameters of the cross-type magnetic coupler.

Symbol	Parameters	Value
l_{P2}×w_{P3}×h_P	Transmitting coil 1 and 2	204×84×2.75mm
l_{P2}×w_{P4}×h_P	Middle coil	204×124×2.75mm
l_{S2}×w_S×h_{S3}	Receiving coil	180×11×87mm
N_P×N_S	Transmitting and receiving coil turns	24×24
3×l_{f2}×w_f×h_f	Rectangular ferrite core	3×34×118×17mm
h	Air gap	2mm

TABLE 5. Parameters of the entire IPT system for UAV.

Parameters	Value
DC voltage source U_{in}/V	84
System working frequency f/kHz	50
The primary self-inductance L_P/μH	80.3
The secondary self-inductance L_S/μH	75.9
Mutual inductance M/μH	25.6
The coupling coefficient k	0.328
The rectifier output power P_{out} /W	131.25-262.5
DC-DC converter input voltage U_L/V	40-48
The primary compensation inductance L_1/μH	39.8
The primary compensation capacitance C_P/nF	255
The compensation capacitance C_1/nF	255
The secondary compensation capacitance C_S/nF	133
The compensation inductance internal resistance R_1/mΩ	78.19
The primary coil internal resistance R_P/mΩ	112.61
The secondary coil internal resistance R_S/mΩ	104.27
The rectifier output equivalent load resistance R_L/Ω	9

uniformity of magnetic field and cost, a plurality of ferrite bars are selected to replace a whole piece of ferrite when the magnetic coupler is actually manufactured, and these ferrite bars are standard. When two ferrite bars are selected to replace the whole piece of ferrite, the magnetic field will be not uniform, which will increase the misalignment sensitivity. When three ferrite bars are selected, the magnetic field will be more uniform and the system misalignment sensitivity will be lower. When four or more ferrite bars are selected that the magnetic field will be more uniform than that of magnetic field with three ferrite bars, but in the later batch production, multiple ferrite bars will increase undoubtedly the assembly difficulty. Therefore, considering synthetically the uniformity of magnetic field and the assembly difficulty, three ferrite bars are selected to replace the whole piece of ferrite in this paper. Each ferrite bar length $l_{f2} = l_f/3 = 34$mm, and the gap l_{f1} between the ferrite bars is 28mm. The cross-type magnetic coupler specific parameters are shown in Table 4.

According to the parameters of magnetic coupler in Table 4, $L_P = 80.3\mu$H, $L_S = 75.9\mu$H and $M = 25.6\mu$H, measured by LCR impedance analyzer. The comparison shows that there is a slight difference between two results mentioned above, which proves the magnetic circuit model is accurate. The specific parameters of the entire IPT system for UAV in Fig. 2 are finally determined as shown in Table 5,

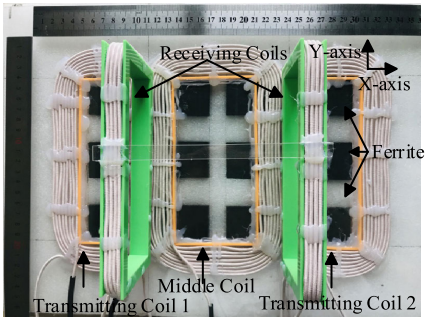

FIGURE 20. Physical diagram of cross-type magnetic coupler.

and based on the data in Table 4, the physical diagram of cross-type magnetic coupler is shown in Fig. 20.

C. MISALIGNMENT TOLERANCE ANALYSIS

The compensation capacitance is calculated according to the system inductance parameter when the magnetic coupler is aligned well. However, when the magnetic coupler is misaligned, the compensation capacitance value will not change. This requires that the L_P and L_S should be kept stable in misalignment so that it cannot affect the system operating state. At the same time, the M reflects the system power transmission capability, which requires M should not be reduced greatly in misalignment, so as to ensure the stability of the rectifier output voltage and output power. Therefore, the L_P, L_S and M are important parameters to represent the system misalignment tolerance capability [26]. The misalignment tolerance of the cross-type magnetic coupler is analyzed in Fig. 20. The curves for the self-inductance and mutual inductance of the cross-type magnetic coupler with misalignment are obtained as shown in Fig. 21.

In Fig. 21, when the magnetic coupler changes from full alignment to misalignment 40mm along the X-axis direction, Y-axis direction and rotation misalignment, the maximum variation of L_P is 0.62μH, 0.61μH and 0.55μH, respectively. The maximum variation of L_S is 1.46μH, 0.35μH and 0.97μH, respectively. Therefore, the misalignment of magnetic coupler has a minor effect on the self-inductance. It will also not affect the system working state. When the magnetic coupler misalignment 25mm along the X-axis direction, misalignment 40mm along the Y-axis direction and rotation misalignment 25°, the M decreases to 17.4μH, 22.8μH and 20.9μH, respectively. At this time, the M change will not have a great effect on the rectifier output voltage and output power. However, when the magnetic coupler along the X-axis direction misalignment is more than 25mm, along the Y-axis direction misalignment is more than 40mm, or rotation misalignment is 25°, the M will be reduced greatly, which will compromise the system power transmission capability. Therefore, the cross magnetic coupler has the misalignment range of X-axis direction [−25mm, 25mm], Y-axis direction [−40mm, 40mm], and rotation [−25°, 25°]. The influence of misalignment on the system will be further discussed later.

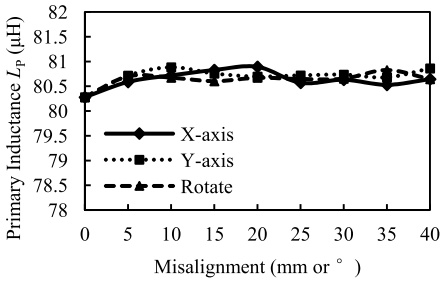

(a) Primary self-inductance

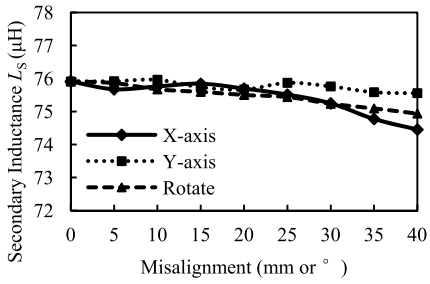

(b) Secondary self-inductance

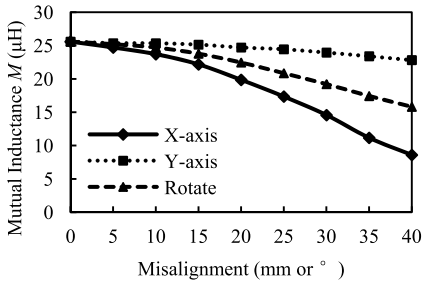

(c) Mutual inductance

FIGURE 21. Parameters variation of magnetic coupler with misalignment.

D. MAGNETIC FIELD ANALYSIS

In this paper, the I_P and I_S of the magnetic coupler should not exceed 12A, and the ampere turns of transmitter pad is set to 408A·N. From Fig. 21, the X-axis direction misalignment has the greatest influence on the system, so the peak magnetic field distributions of the cross-type magnetic coupler considering complete alignment and the X-axis direction maximum misalignment position are obtained by ANSYS Maxwell software for 3D simulation as shown in Fig. 22.

From Fig. 22, the magnetic field distribution is consistent with the modeling analysis of the magnetic coupler mentioned above. The peak magnetic field distributions of the misalignment case is not much different from that of the complete alignment case. But in the case of misalignment, the main flux will be decreased and the leakage flux will be increased, which is also the main reason for the decrease of the M and k. When the height is greater than 121mm, the flux density of magnetic coupler is less than 1×10^{-5}T. Therefore, it will not cause the damage to UAV's internal equipment by

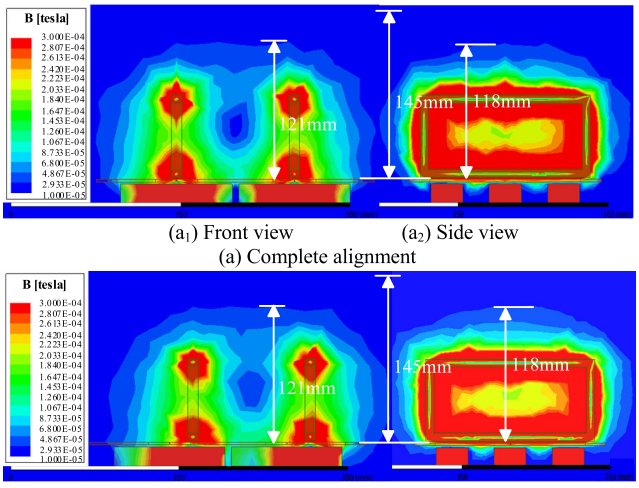

FIGURE 22. Peak magnetic field distribution of the cross-type magnetic coupler.

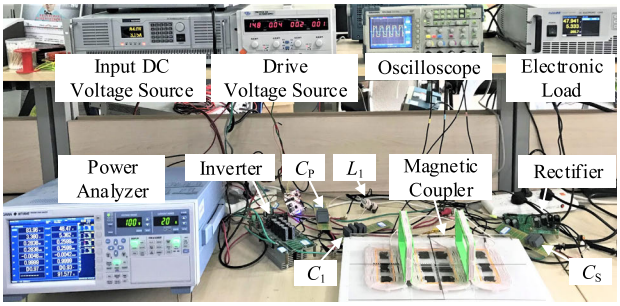

FIGURE 23. IPT system experimental platform.

high frequency magnetic field. The saturation of the magnetic core will cause the magnetic coupler temperature rising and the core loss increasing, so the saturation of the magnetic core should be considered in the design for wireless charging system. The PC40 ferrite core material of TDK company is used in this paper, whose saturation flux is 0.51T at 25°C, but the peak flux density of magnetic coupler is 3×10^{-4}T which is much lower than the saturation flux density. Therefore, the problem of saturation of the magnetic core will not occur.

V. EXPERIMENTAL VERIFICATION

The IPT system experimental platform with a cross-type magnetic coupler is shown in Fig. 23. It contains an input DC voltage source, a drive voltage source, a DSP controller core board, an inverter circuit, a magnetic coupler, a compensation inductance, three compensation capacitances, a rectifier circuit, an electronic load, an oscilloscope and a power analyzer. The input voltage is 84V, the inverter working frequency is 50kHz, the load resistance R_L of rectifier is 9Ω, and the cross-type magnetic coupler works in a well-aligned condition.

The inverter output voltage and current and the rectifier input voltage and current waveform considering complete

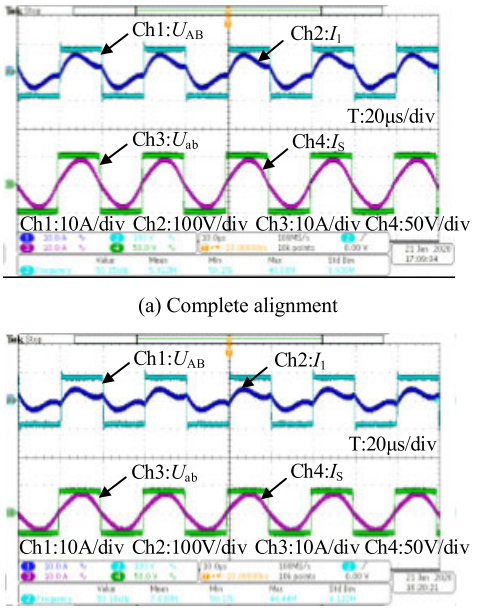

FIGURE 24. Voltage and current waveform of Inverter output and rectifier input.

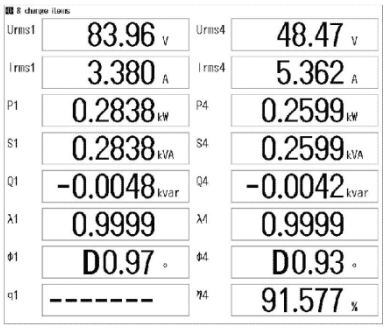

FIGURE 25. IPT system experimental result. P_1 is system input power, P_4 is rectifier output power, η_4 is IPT system efficiency.

alignment and the maximum position of the X-axis direction misalignment are shown in Fig. 24.

It can be seen that the output voltage and current of the maximum tolerated misalignment position of the X-axis direction are in the same phase compared with the complete alignment, indicating that the system is still in a resonant state. The system power transfer capability is tested by using power analyzer as shown in Fig. 25. The rectifier output power P_{out} is 259.9W and the IPT system efficiency η_{out} is 91.577%. When the charging voltage for lithium battery reaches the maximum charging voltage U_{bmax}, the duty cycle of the switch S_5 D = 25.2V/48.47V=0.52, the charging current for lithium battery I_b = 5.362A/0.52=10A which is the maximum charging current for lithium battery I_{bmax}, which meets the requirement of maximum charging power point for lithium battery. It can ensure that when the magnetic coupler is in a well-aligned operating condition, adjusting the duty cycle D can make the system maintain a constant maximum charging current I_{bmax} to charge lithium battery

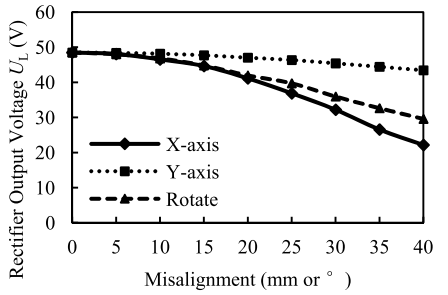

(a) U_L misalignment test

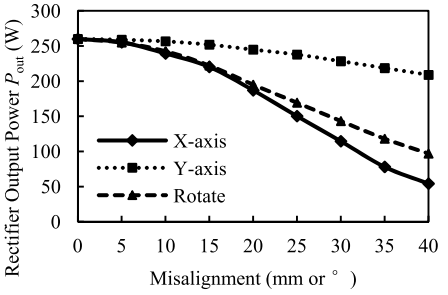

(b) P_{out} misalignment test

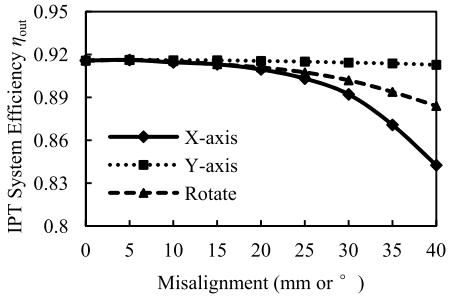

(c) η_{out} misalignment test

FIGURE 26. Misalignment test results.

quickly until the maximum charging voltage U_{bmax}. Therefore, the experimental system can be used to charge UAV wirelessly.

When the rectifier output equivalent load resistance R_L is 9Ω, the system misalignment test is carried out, with test results shown in Fig. 26.

In Fig. 26, when the magnetic coupler is displaced from alignment to X-axis direction misalignment 25mm, the rectifier output voltage U_L variation range is 36.85-48.47V, the rectifier output power P_{out} variation range is 150.2-259.9W, and the IPT system efficiency η_{out} variation range is 90.314%-91.577%. When the magnetic coupler is displaced from alignment to Y-axis direction misalignment 40mm, U_L variation range is 43.41-48.47V, P_{out} variation range is 208.8-259.9W, and η_{out} variation range is 91.282%-91.577%. When the magnetic coupler is displaced from alignment to rotation misalignment 25°, U_L variation range is 39.69-48.47V, P_{out} variation range is 169.3-259.9W, and η_{out} variation range is 90.75%-91.577%. All of the above meet the requirements of UAV wireless charging. Therefore, the misalignment tolerance capability of IPT system is set as X-axis direction [−25mm, 25mm], Y-axis direction [−40mm, 40mm], and rotation misalignment [−25°, 25°].

VI. CONCLUSION

At first, a cross-type magnetic coupler for UAV has been proposed in this paper, which has restrained effectively the magnetic field height. Secondly, The system magnetic circuit and electric circuit models have been established, whilst a simple and practical iterative method for optimizing the magnetic coupler geometry parameters has been proposed. Then the geometry parameters of the cross-type magnetic coupler have been calculated which have met the charging requirements of lithium battery. It has shown that the magnetic coupler could restrain the magnetic field effectively within the 145mm height above the transmitter pad and avoid the influence of high frequency magnetic field on UAV's internal equipment. At last, the experimental system has been built, and the system misalignment tolerance capability has been obtained. It has been verified that the system can transfer 260W power with the IPT system efficiency of 91.577%. The model can be used to guide the wireless charging system design for special applications and special requirements for magnetic coupler, which refer to the limitation of the space occupied by the magnetic coupler and the strict limitation of the magnetic field height.

REFERENCES

[1] P. Skorput, S. Mandzuka, and H. Vojvodic, "The use of unmanned aerial vehicles for forest fire monitoring," in *Proc. Int. Symp. (ELMAR)*, Sep. 2016, pp. 93–96.

[2] I. Zacarias, J. Schwarzrock, L. P. Gaspary, A. Kohl, R. Q. A. Fernandes, J. M. Stocchero, and E. P. de Freitas, "Employing SDN to control video streaming applications in military mobile networks," in *Proc. IEEE 16th Int. Symp. Netw. Comput. Appl. (NCA)*, Oct. 2017, pp. 1–4.

[3] S. Kim, A. Zaheer, and G. Covic, "Tripolar pad for inductive power transfer systems," *IEEE Trans. Power Electron.*, vol. 32, no. 7, pp. 5045–5057, 2017.

[4] T. Kan, R. Mai, P. P. Mercier, and C. C. Mi, "Design and analysis of a three-phase wireless charging system for lightweight autonomous underwater vehicles," *IEEE Trans. Power Electron.*, vol. 33, no. 8, pp. 6622–6632, Aug. 2018.

[5] Y.-H. Zhang, Y.-C. Lin, S.-X. Lin, W.-Z. Gao, L.-B. Chen, W.-J. Chang, W.-W. Hu, and C.-T. Yu, "An implementation of an automatic adjustment power transfer position wireless battery charging system for mobile devices," in *Proc. IEEE 6th Global Conf. Consum. Electron. (GCCE)*, Oct. 2017, pp. 1–2.

[6] X. Meng, D. Qiu, M. Lin, S. C. Tang, and B. Zhang, "Output voltage identification based on transmitting side information for implantable wireless power transfer system," *IEEE Access*, vol. 7, pp. 2938–2946, 2019.

[7] S. Kumar and G. K. M. Jayprakash, "Wireless power transfer for unmanned aerial vehicle (UAV) charging," *Int. Res. J. Eng. Technol.*, vol. 8, no. 8, p. 1939, 2017.

[8] D. Ke, C. Liu, C. Jiang, and F. Zhao, "Design of an effective wireless air charging system for electric unmanned aerial vehicles," in *Proc. 43rd Annu. Conf. IEEE Ind. Electron. Soc. (IECON)*, Oct. 2017, pp. 6949–6954.

[9] T. Campi, S. Cruciani, M. Feliziani, and F. Maradei, "High efficiency and lightweight wireless charging system for drone batteries," in *Proc. AEIT Int. Annu. Conf.*, Sep. 2017, pp. 1–6.

[10] K. Sang-Won, C. In-Kui, and H. Sung-Yong, "Comparison of charging region differences according to receiver structure in drone wireless charging system," in *Proc. Int. Conf. Inf. Commun. Technol. Converg. (ICTC)*, Oct. 2017, pp. 1058–1060.

[11] A. B. Junaid, Y. Lee, and Y. Kim, "Design and implementation of autonomous wireless charging station for rotary-wing UAVs," *Aerosp. Sci. Technol.*, vol. 54, pp. 253–266, Jul. 2016.
[12] C. Cai, S. Wu, M. Qin, and Z. Yang, "A novel magnetic coupler for unmanned aerial vehicle wireless charging systems," in *Proc. IEEE Int. Power Electron. Appl. Conf. Exposit. (PEAC)*, Nov. 2018, pp. 1–5.
[13] H. Zeng, Z. Liu, Y. Hou, T. Hei, and B. Zhou, "Optimization of magnetic core structure for wireless charging coupler," *IEEE Trans. Magn.*, vol. 53, no. 6, pp. 1–4, Jun. 2017.
[14] W. Zhang, S.-C. Wong, C. K. Tse, and Q. Chen, "Analysis and comparison of secondary series- and parallel-compensated IPT systems," in *Proc. IEEE Energy Convers. Congr. Exposit.*, Sep. 2013, pp. 2898–2903.
[15] Y. Zhang, K. Chen, F. He, Z. Zhao, T. Lu, and L. Yuan, "Closed-form oriented modeling and analysis of wireless power transfer system with constant-voltage source and load," *IEEE Trans. Power Electron.*, vol. 31, no. 5, pp. 3472–3481, May 2016.
[16] H. Hao, G. A. Covic, and J. T. Boys, "An approximate dynamic model of LCL-*T*-based inductive power transfer power supplies," *IEEE Trans. Power Electron.*, vol. 29, no. 10, pp. 5554–5567, Oct. 2014.
[17] S. Li, W. Li, J. Deng, T. D. Nguyen, and C. C. Mi, "A double-sided LCC compensation network and its tuning method for wireless power transfer," *IEEE Trans. Veh. Technol.*, vol. 64, no. 6, pp. 2261–2273, Jun. 2015.
[18] M. Budhia, G. A. Covic, and J. T. Boys, "Design and optimization of circular magnetic structures for lumped inductive power transfer systems," *IEEE Trans. Power Electron.*, vol. 26, no. 11, pp. 3096–3108, Nov. 2011.
[19] G. A. Covic and J. T. Boys, "Modern trends in inductive power transfer for transportation applications," *IEEE J. Emerg. Sel. Topics Power Electron.*, vol. 1, no. 1, pp. 28–41, Mar. 2013.
[20] ICNIRP, "Guidelines for limiting exposure to time-varying electric and magnetic fields (1 Hz to 100 kHz)," *Health Phys*, vol. 99, no. 6, pp. 818–836, 2010.
[21] M. Budhia, J. T. Boys, G. A. Covic, and C.-Y. Huang, "Development of a single-sided flux magnetic coupler for electric vehicle IPT charging systems," *IEEE Trans. Ind. Electron.*, vol. 60, no. 1, pp. 318–328, Jan. 2013.
[22] G. He, Q. Chen, X. Ren, S.-C. Wong, and Z. Zhang, "Modeling and design of contactless sliprings for rotary applications," *IEEE Trans. Ind. Electron.*, vol. 66, no. 5, pp. 4130–4140, May 2019.
[23] H. Hao, G. Covic, and M. Kissin, "A parallel topology for inductive power transfer power supplies," in *Proc. IEEE Appl. Power Electron. Conf. Expo.*, Mar. 2011, pp. 2027–2034.
[24] R. L. Steigerwald, "A comparison of half-bridge resonant converter topologies," *IEEE Trans. Power Electron.*, vol. PEL-3, no. 2, pp. 174–182, Apr. 1988.
[25] S. Chopra and P. Bauer, "Driving range extension of EV with on-road contactless power Transfer—A case study," *IEEE Trans. Ind. Electron.*, vol. 60, no. 1, pp. 329–338, Jan. 2013.
[26] Z. Li, C. Zhu, J. Jiang, K. Song, and G. Wei, "A 3-kW wireless power transfer system for sightseeing car supercapacitor charge," *IEEE Trans. Power Electron.*, vol. 32, no. 5, pp. 3301–3316, May 2017.

CHUNWEI CAI (Member, IEEE) was born in Shandong, China, in 1977. He received the B.S. and M.S. degrees in control theory and control engineering from Shandong University, Jinan, China, in 2001 and 2004, respectively, and the Ph.D. degree in electrical engineering from the Harbin Institute of Technology (HIT), Harbin, China, in 2013. He has been a Lecturer, since 2006, and has been an Assistant Professor, since 2014, with HIT, Weihai, China. His current research interests include wireless power transfer systems, power converters, and inverters.

JINQUAN LIU was born in Heilongjiang, China, in 1995. He received the B.S. degree in electrical engineering and automation from Zhengzhou University, Zhengzhou, China, in 2018. He is currently pursuing the M.S. degree in electrical engineering with the School of New Energy, Harbin Institute of Technology (HIT), Weihai, China. His current research interests include power electronics and wireless power transfer system for unmanned aerial vehicle.

SHUAI WU received the B.S. degree in electrical engineering and automation from Shanxi Agricultural University, Jinzhong, China, in 2017, and the M.S. degree in electrical engineering from the Harbin Institute of Technology, Weihai, China, in 2019, where he is currently pursuing the Ph.D. degree. His current research interests include wireless power transfer for autonomous underwater vehicles and unmanned aerial vehicles.

YANYU ZHANG was born in Jiangsu, China, in 1995. He received the B.S. degree in electrical engineering and automation from the China University of Mining and Technology, Xuzhou, China, in 2018. He is currently pursuing the M.S. degree in electrical engineering with the School of New Energy, Harbin Institute of Technology (HIT), Weihai, China. His current research interests include power electronics and wireless power transfer system for autonomous underwater vehicle.

LONGYUN JIANG was born in Shandong, China, in 1997. He received the B.S. degree in electrical engineering and automation from the Qingdao University of Technology, Qingdao, China, in 2019. He is currently pursuing the M.S. degree in electrical engineering with the School of New Energy, Harbin Institute of Technology (HIT), Weihai, China. His current research interests include power electronics and wireless power transfer system for unmanned aerial vehicle.

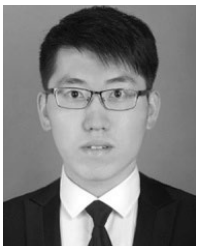

ZHIPENG ZHANG was born in Shanxi, China, in 1993. He received the B.S. degree in electrical engineering and automation from Yanshan University, Qinhuangdao, China, in 2016. He is currently pursuing the M.S. degree in electrical engineering with the School of New Energy, Harbin Institute of Technology (HIT), Weihai, China. His current research interests include power electronics and wireless power transfer system for autonomous underwater vehicles.

JINPENG YU (Member, IEEE) received the B.Sc. degree in automation from Qingdao University, Qingdao, China, in 2002, the M.Sc. degree in system engineering from Shandong University, Jinan, China, in 2006, and the Ph.D. degree from the Institute of Complexity Science, Qingdao University, in 2011. He is currently a Distinguished Professor with the School of Automation, Qingdao University. His research interests include electrical energy conversion and motor control, applied nonlinear control, and intelligent systems. He was a recipient of the Shandong Province Taishan Scholar Special Project Fund and the Shandong Province Fund for Outstanding Young Scholars.